A. Wave propagation over uneven bottoms in 2DH

A.1. *Wave propagation over an elliptical shoal on a sloping bottom*

The laboratory experiment of wave propagation over an elliptical shoal on a sloping bottom (Berkhoff *et al.* 1982) is a classic case to validate the performance of numerical models in simulating waves interacting with three-dimensional submerged structures (e.g. Wei *et al.* 1999; Ma *et al.* 2012). The experiment was conducted in a wave tank of 20 m in width and 22 m in length. A contour plot of the bottom topography is shown in figure 1. Let (x', y') be the slope-oriented coordinates, an elliptic shoal centered at $x' = 0$ and $y' = 0$ is constructed on a constant slope of 1/50, which are related to the (x, y) coordinate system by rotating 20°. The still water depth without the shoal is

$$\left.\begin{aligned} &h = 0.45 \qquad x' < -5.84, \\ &h = max(0.07, 0.45 - 0.02(5.84 + x')) \qquad x' \geq -5.84, \end{aligned}\right\} \tag{A.1}$$

and the minimum water depth is 0.07 m. The boundary of the shoal is given by

$$(\frac{x'}{3})^2 + (\frac{y'}{4})^2 = 1, \tag{A.2}$$

and the thickness of the shoal is

$$d_s = -0.3 + 0.5\sqrt{1 - (\frac{x'}{3.75})^2 - (\frac{y'}{5})^2}. \tag{A.3}$$

The incident wave has an amplitude of 2.32 cm with a period of 1.0 s in a water depth of 0.45 m, which corresponds to waves in finite water depth with $kh \approx 1.9$ and weak nonlinearity of $ka \approx 0.098$. Wave height data are collected along eight transects as shown in figure 1. In the numerical simulations, the spatial and temporal resolutions are $\Delta x = 0.05$ m, $\Delta y = 0.10$ m, and $\Delta t = 0.03$ s. A sponge layer is employed downstream to absorb outgoing waves. Free-slip boundary conditions are applied at the two sidewalls which are located at $y = -10$ m and $y = 10$ m, respectively. The numerical simulation is carried out for 33 s and the last four waves are used for calculating the wave heights. Additional tests show that the $S2$ model already produces converged results for this case.

The comparisons of wave heights along eight transects between numerical results and experimental data are shown in figure 2. Waves reach maximum wave height at section (3) behind the elliptic shoal, which is more than twice the incident wave height. Although the model slightly underestimates the maximum wave height at transects (3) and (5), the overall spatial variations of wave heights are well captured by the numerical model, which demonstrates the ability of present models in simulating wave refraction and diffraction phenomena.

A.2. *Wave propagation over a semi-circular shoal*

Whalin (1971) conducted a set of experiments to study wave train shoaling and focusing behind a semi-circular shoal. The experiments were performed in a wide wave flume of 25.6 m long and 6.096 m wide. The still water depth is 0.4572 m at the incident wave boundary and decreases to 0.1524 m at the end of the flume. A semi-circular shoal was constructed in the middle of the wave flume. Let (x, y) be the coordinates in the alongshore and cross-shore direction, respectively, the bottom bathymetry can be described as:

$$h = \begin{cases} 0.4572, & 0 \leq x \leq 10.67 - T(y) \\ 0.4572 + (10.67 - G(y) - x)/25), & 10.67 - T(y) \leq x \leq 18.29 - T(y) \\ 0.1524, & 18.297 - T(y) \leq x \end{cases} \tag{A.4}$$

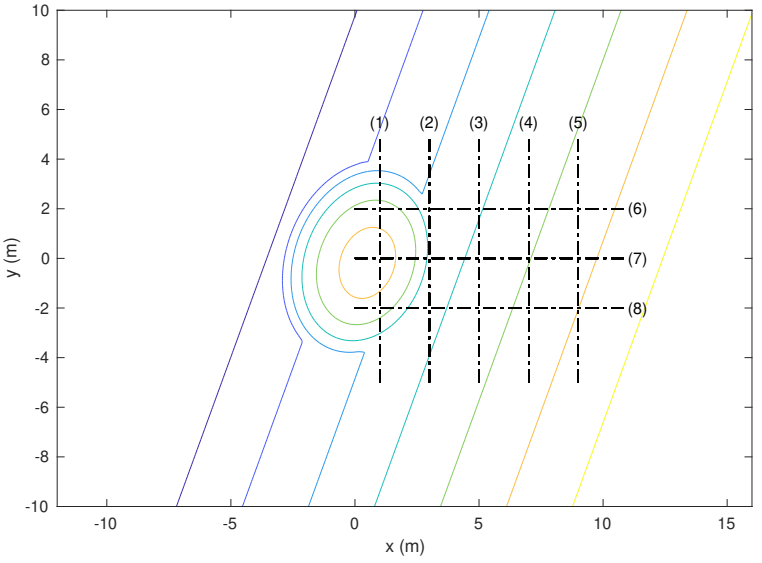

FIGURE 1. Bottom bathymetry and locations of measurement transects for wave propagation over an elliptical shoal on a sloping bottom. (Berkhoff *et al.* 1982).

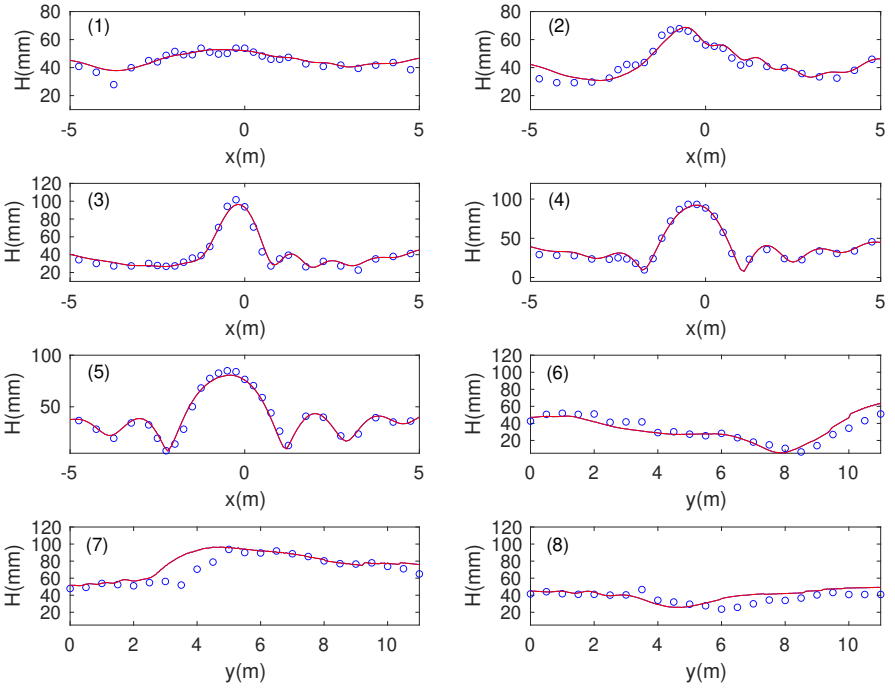

FIGURE 2. Comparisons of wave heights along eight transects between numerical results from $S2$ model (red line) and experimental data (blue circles).

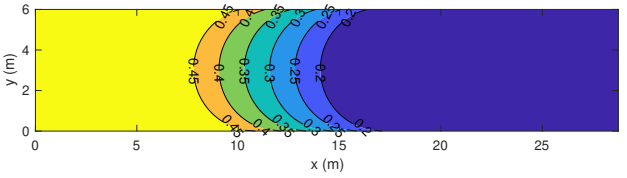

FIGURE 3. Bottom bathymetry for wave propagation over a semi-circular shoal (Whalin 1971).

Case	wave amplitude (m)	period (s)	kh	H/h	Δx	Δt
(1)	0.0195	1	1.92	0.0853	0.05	0.025
(2)	0.0075	2	0.73	0.0328	0.1	0.06
(3)	0.0068	3	0.47	0.0297	0.15	0.1

TABLE 1. Incident wave conditions and numerical parameters in Whalin (1971).

with $T(y) = \sqrt{y(6.096 - y)}$. The contour plot of the bottom bathymetry is shown in figure 3. Three cases with different incident wave conditions are considered here, which are summarized in table 1. Free surface elevations are collected along the centre line of the wave flume, from which the amplitudes of the first three harmonics are obtained.

The spatial and temporal resolutions used in the numerical simulations are summarized in table 1. While a sponge layer is implemented at the end of the flume to absorb outgoing waves, free-slip boundary conditions are used along the lateral boundaries. Numerical simulations are carried out using the $S2$ model while models of higher approximation do not produce noticeable differences. The upper panels in figures 4 to 6 show the instantaneous free surface elevations at the end of each numerical simulation for cases 1 to 3. The original plane waves shoal as they propagate on the slope and three-dimensional features appear because of the semi-circular bottom bathymetry. Wave focusing is also observed behind the shoal in the shallower water region.

The comparisons of wave amplitudes of the first three harmonics along the center of the wave flume are shown in lower panels of figures 4 to 6. The wave amplitude of each harmonic is obtained by a Fourier analysis on the last ten waves in the numerical simulations, and it has been tested that ten waves are sufficient for the analysis performed here. The incident waves are uniform single harmonic waves, however, in the presence of the circular shoal, wave heights are significantly amplified because of the shoaling effect. Higher harmonics are generated during this process and their amplitudes become evident as waves propagating onto the shoal.

Although case 1 has the largest kh value and thus the strongest dispersive effects, the $S2$ model is still able to provide reasonable predictions on the spatial variations of

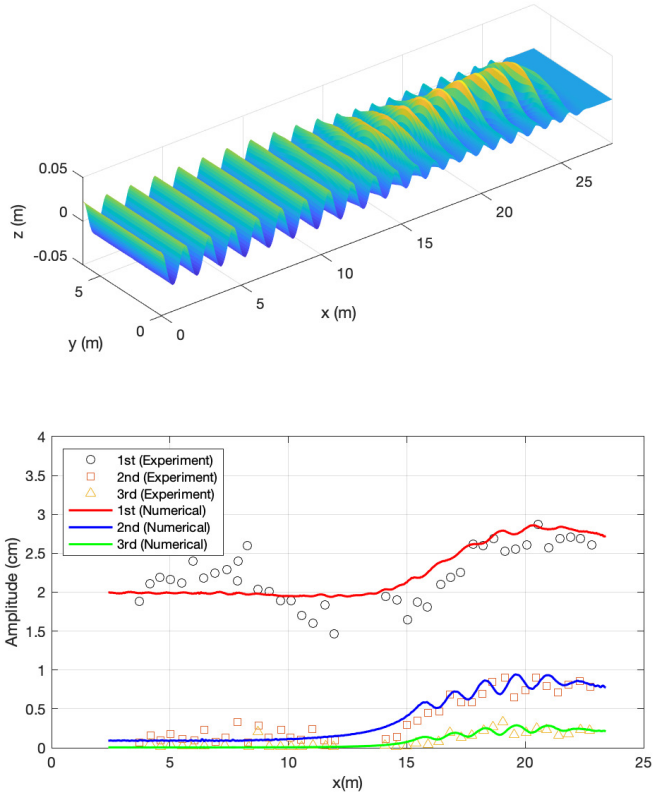

FIGURE 4. Upper panel: Instantaneous free surface elevations at $t = 40$ s for case 1. Lower panel: Comparison of wave amplitudes of different harmonics along the center of the flume for case 1.

the amplitude of each harmonic. Although the incident wave in case 3 has a relatively small kh value, the agreement between the experimental data and numerical results is less satisfactory, with the first harmonic being overestimated and higher harmonics being underestimated. This phenomenon has also been reported by several previous numerical studies (Kazolea *et al.* 2012; Lannes & Marche 2015), which may be caused by the reflected waves in the laboratory experiments because of relatively long incident wavelengths.

A.3. *Solitary wave runup on a conical island*

A series of laboratory experiments was conducted by Briggs *et al.* (1994) to study breaking and non-breaking solitary wave runup on a conical island, which has been widely used for the validation of wave runup models (e.g. Liu *et al.* 1995; Titov & Synolakis 1998; Lynett *et al.* 2002; Choi *et al.* 2007; Fuhrman & Madsen 2008). In the present 2DH model, the method of two-dimensional linear regression to determine values at dry nodes successively developed by Fuhrman & Madsen (2008) is implemented in present models to simulate the wave runup phenomena.

The physical experiment was carried out in a wave basin of 25 m×30 m with a water depth of 0.32 m, where a conical island is constructed near the center of the wave basin

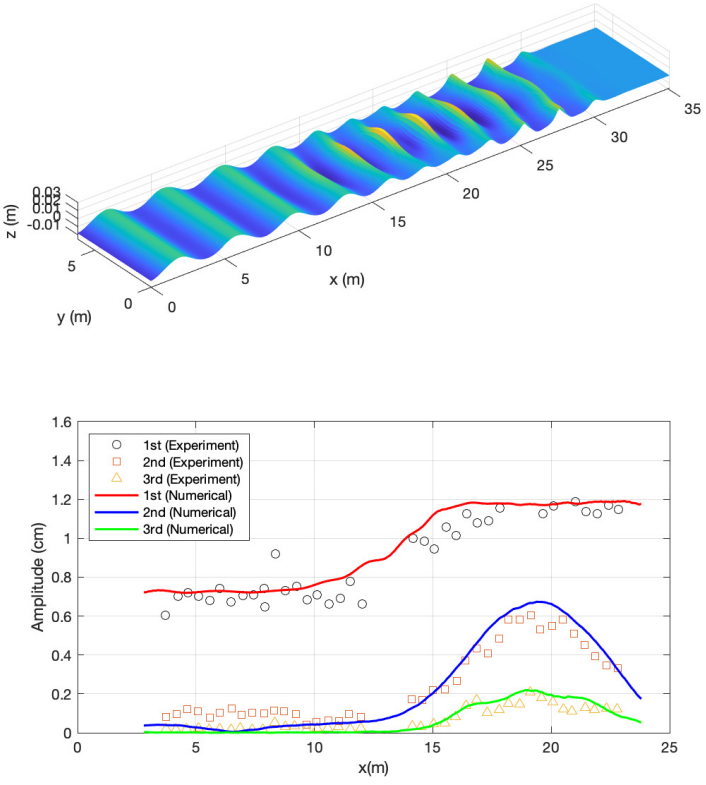

FIGURE 5. Upper panel: Instantaneous free surface elevations at $t = 50$ s for case 2. Lower panel: Comparison of wave amplitudes of different harmonics along the center of the flume for case 2.

with a base diameter of 7.2 m, a top diameter of 2.2 m, and a side slope of 1:4. A three-dimensional view of the experimental setup can be found in the left panel of figure 7. Two non-breaking solitary wave cases are simulated here, i.e. case A and case B, which correspond to solitary wave heights of 0.013 m and 0.028 m and nonlinearity of 0.04 and 0.09, respectively. Several wave gauges are deployed around the island to measure the time series of free surface elevations.

In the numerical simulations, the computational domain is 30×30 m with the center of the island located at $x = 18$ m, $y = 15$ m. The solitary wave is initially centered at $x = 8$ m, propagating in the positive x direction. Sponge layers of 1 m and 4 m are arranged at the upstream and downstream boundary, while the no-flux boundary condition is imposed on two side walls. A uniform grid of $\Delta x = \Delta y = 0.2$ m and 0.15 m are used for case A and case B, respectively, while the time step is 0.1 s for both cases. The free surface elevations are collected at four wave gauge stations. While wave gauge 6 is located at the front of the island near the island base, wave gauges 9, 16, and 22 are located near the initial shoreline position and are on the front, side, and back of the island as shown in the right panel of figure 7. Figure 8 shows the comparison of surface elevations between numerical and experimental results at four stations for case A and

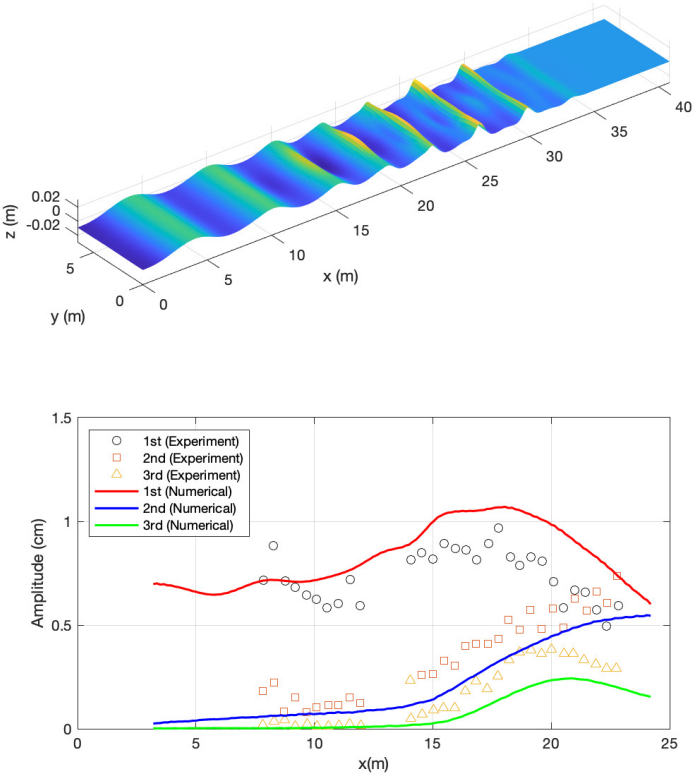

FIGURE 6. Upper panel: Instantaneous free surface elevations at $t = 50$ s for case 3. Lower panel: Comparison of wave amplitudes of different harmonics along the center of the flume for case 3.

case B. The overall agreement is good with both the leading wave and surface depression being well predicted by the numerical model.

A.4. *Irregular wave propagation over a submerged shoal*

Vincent & Briggs (1989) conducted laboratory experiments to compare the behavior of monochromatic waves and directional spreading irregular waves transformation over a submerged elliptical shoal, which have been widely used for the validations of three-dimensional wave models, e.g., parabolic-type wave model (Pancbang *et al.* 1990; Chawla *et al.* 1998), spectral wave model (Mase 2001; Holthuijsen *et al.* 2003; Ding *et al.* 2006), Boussinesq type models Lynett & Liu (2004), and non-hydrostatic models (Yuan & Wu 2005). In this section, the present 2DH numerical model is further validated using this set of experimental data to test its performance in simulating irregular waves in three dimensions.

The laboratory experiments were conducted in a wave basin that is 35 m in width and 29 m in length. An elliptical shoal with a major radius of 3.96 m and a minor radius of 3.05 m is constructed on the flat bottom. The boundary of the shoal and the elevation

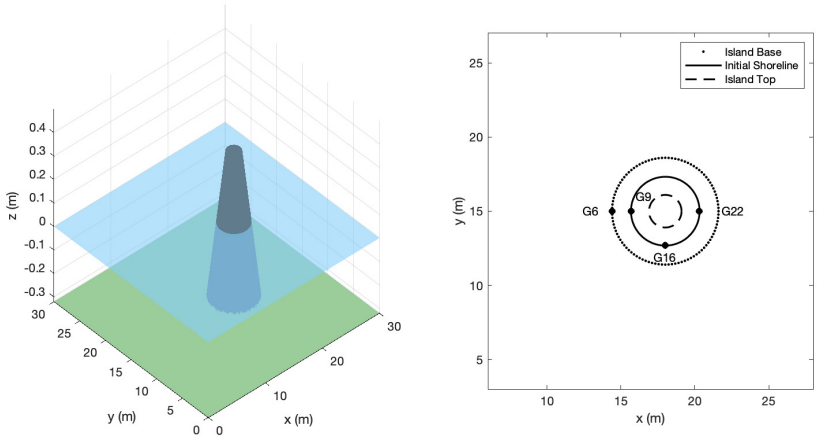

FIGURE 7. Left panel: three-dimensional view of the experimental setup in Briggs *et al.* (1994). Right panel: locations of the measurement gauges.

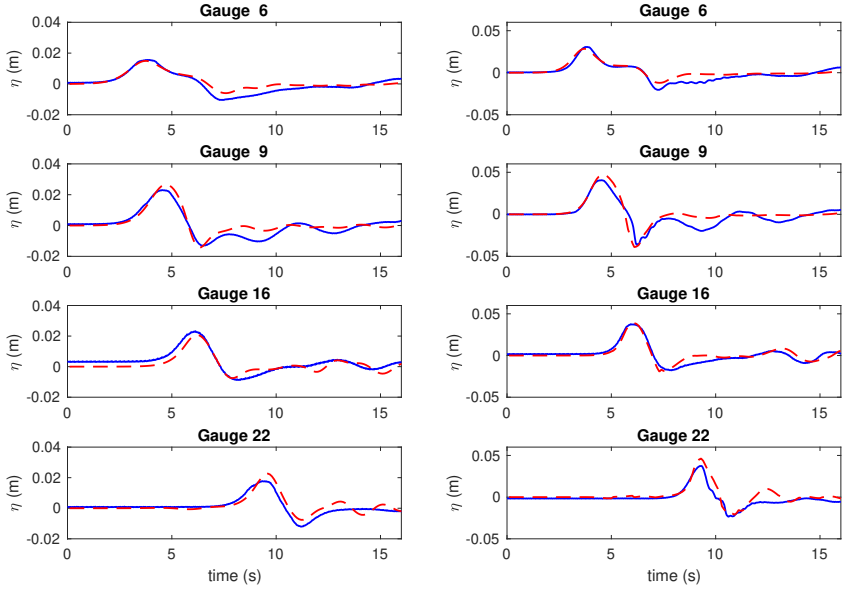

FIGURE 8. Comparisons of free surface elevations between numerical results (red dashed line) and experimental data (blue lines) for case A (left panel) and case B (right panel).

at any point in the shoal cross-section can be described as

$$(\frac{X'}{3.05})^2 + (\frac{Y'}{3.96})^2 = 1, \tag{A.5}$$

$$h = -0.4572 + 0.7620\Big\{1 - (\frac{X'}{3.81})^2 - (\frac{Y'}{4.95})^2\Big\}^{0.5},$$

where X', Y' are localized coordinates centered on the shoal denoting minor and major

Case ID	T(s)	H_0(cm)	$\alpha[-]$	$\gamma[-]$	σ_θ
U3	1.3	2.54	0.00155	2	0
N3	1.3	2.54	0.00155	2	10
B3	1.3	2.54	0.00155	2	30

TABLE 2. Incident wave conditions in Vincent & Briggs (1989). T, (peak) wave period; H_0, (significant) wave height; α, Phillips constant; γ, peak enhancement factor; σ_θ, directional spreading standard deviation.

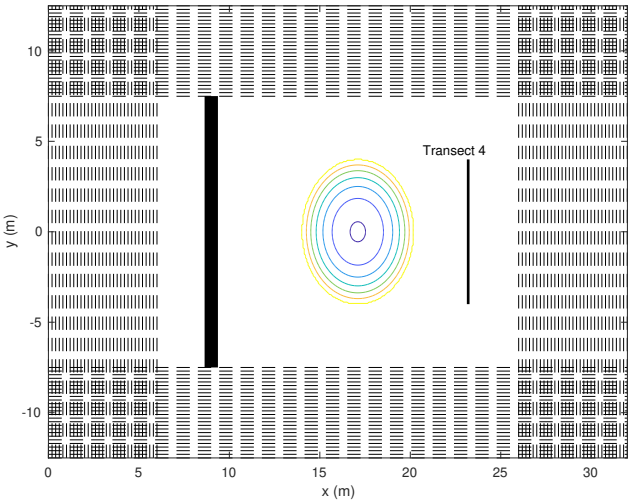

FIGURE 9. Numerical setup of irregular wave propagation over a submerged shoal (Vincent & Briggs 1989).

axes, respectively. The still water depth is 0.4572 m and the water depth at the center of the shoal is 0.1524 m.

Three cases of different incident wave conditions are selected here to reproduce numerically, i.e., case U3, N3, and B3, which represent unidirectional waves, narrowly and broadly distributed directionally spreading waves, respectively. The detailed incident wave conditions are summarised in table 2. We remark here that these three cases are relatively more challenging because their frequency spectra have the smallest peakedness value ($\gamma = 2$) for the TMA shallow water spectrum (Bouws *et al.* 1985) among all laboratory cases. The peak wave period is 1.3 s corresponding to $kh \approx 1.27$, and the target wave height is 2.54 cm for both cases. It should be noted that because of the board distribution (or small peakedness value) of the frequency spectrum, there are appreciable relatively high-frequency wave components up to $kh \approx 3.0$. In terms of the directional wave case, the directional spectrum function used in case N3 and B3 follows a wrapped normal distribution with a directional spreading parameter of $\sigma_m = 10.0°$ and $\sigma_m = 30.0°$, respectively. Goda (2000) suggested that at least 200 waves at the peak wave period are needed to obtain reliable statistical information for the random wave field. Thus, the total simulation time is set to be 280 s.

The numerical setup is sketched in figure 9, where locations of the wave generation region (thick black line), sponge layers (dashed areas), location of the shoal (contour

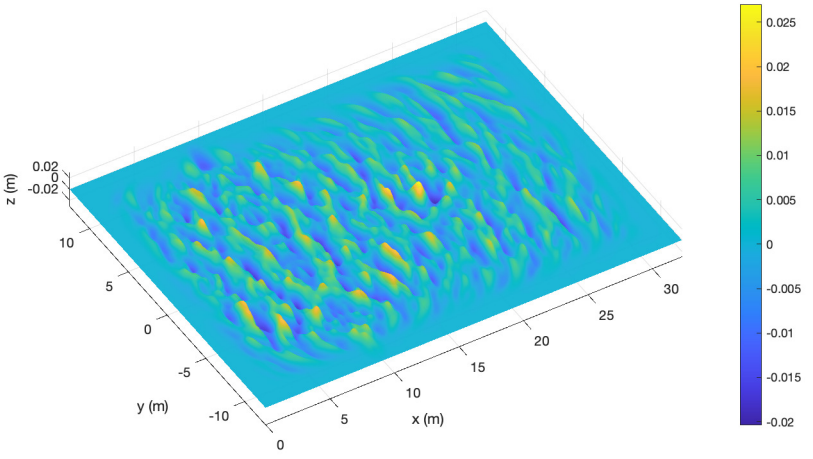

FIGURE 10. Numerical results of free surface elevations at $t = 280$ s for case B3.

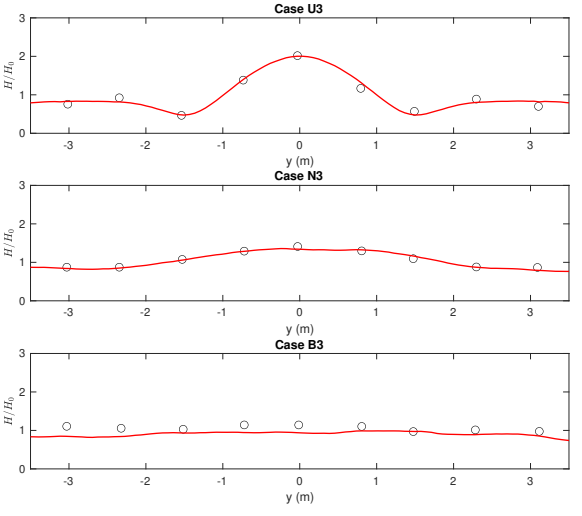

FIGURE 11. Comparisons of significant wave heights between numerical results (red line) and experiment data (black circles) at transect 4 for three cases.

lines in color), and the transect for free surface elevations collection are denoted in the figure. The center of the shoal is located at $x = 17.2$ m, $y = 0$ m. A spatial resolution of 0.07 m in both $x-$ and $y-$ directions and a temporal resolution 0.035 s are used in the numerical simulations. For the irregular wave generation, the wave spectra are divided into 100 frequency components with equal wave energy. The directional components are then evenly split in each frequency. The $S2$ model is used to carry out the simulations for all three cases.

For brevity, only the instantaneous free surface elevations at the end of the numerical simulations, i.e., $t = 280$ s for case B3 are shown in figure 10. For the unidirectional incident wave case (U3), because of the combined effect of wave refraction, shoaling, and diffraction induced by the submerged obstacle, waves focus behind the shoal and the wave field shows three-dimensional patterns. However, for the directional spreading

Case	Amplitude	Depth	Period	kh	ka	Current profile	Relative current strength
(1)	35.1 mm	0.35 m	1.412 s	0.88	0.09	uniform, 0.108 m/s	0.066
(2)	35.7 mm	0.45 m	0.877 s	2.91	0.23	uniform, -0.120 m/s	-0.089
(3)	61.5 mm	0.35 m	1.42 s	1.22	0.21	linear, -0.480 m/s	-0.29

TABLE 3. Waves and current conditions in Swan (1990).

incident waves (N3 and B3), the focusing effect behind the shoal is much less obvious compared with the unidirectional case as the wave energy is being distributed in several directions.

Figure 11 shows the comparison of significant wave heights between the laboratory experiments and numerical results at the measurement transect 4. The significant wave height is calculated by a wave-by-wave analysis on the time series free surface elevations for 200 (peak) wave periods. The agreements between the numerical results and experimental data are reasonably good for all three cases, demonstrating the capability of present models in simulating irregular wave propagation over uneven bathymetry. It can be observed that the wave height is being significantly amplified for the unidirectional irregular wave case (U3), reaching approximately twice the incident wave height. However, when it comes to directional spreading incident waves, the directionality of incident waves strongly weakens this phenomenon. While the wave focusing behind the shoal can be still observed for the narrowly spreading case (N3), the wave heights behind the shoal are almost the same as the incident wave height for the broadly spreading case (B3).

B. Finite amplitude periodic waves on uniform or linearly sheared currents

In this section, the present models are further validated by a set of laboratory experiments of wave–current interactions, in which the waves are weakly nonlinear and the currents have either a uniform or linear profile in the water column (Swan 1990). This set of data has been used for validating the linear mild-slope equations for waves on currents with constant horizontal vorticity (Touboul *et al.* 2016) and Boussinesq-type of models for wave–current interactions (Son & Lynett 2014). The focus of the validation is not only on the free surface elevation but also on the fluid particle velocity.

Three experimental cases are selected for validations ($ka = 0.09 - 0.23$ and $kh = 0.88 - 2.91$), which are summarized in table 3. The wavenumber, k, is calculated from the frequency dispersion relation for a linear wave with the consideration of current. The current profiles and surface current velocities are also listed in the table. The relative current strength in the last column of table 3 is specified as the ratio between the current velocity at the free surface and wave celerity; the sign indicates whether the wave and current are moving in the same (positive) or opposite (negative) direction. In cases 1 and 2 currents are uniform in the water column, and the current strengths are relatively weak. On the other hand, in case 3 the current has a linear profile in the vertical direction with a constant shear of -1.71 s^{-1} and its strength is moderate. The laboratory measurements of the current profile (case 3) without waves are denoted by $*$ in figure 12(a), and the linear interpolation result, which is used by u^* in the present model, is shown by the blue line in the same figure.

Similar to §4.1.1 in the main body of the paper, an internal wavemaker located close to the left boundary is employed to generate and propagate waves into the current region.

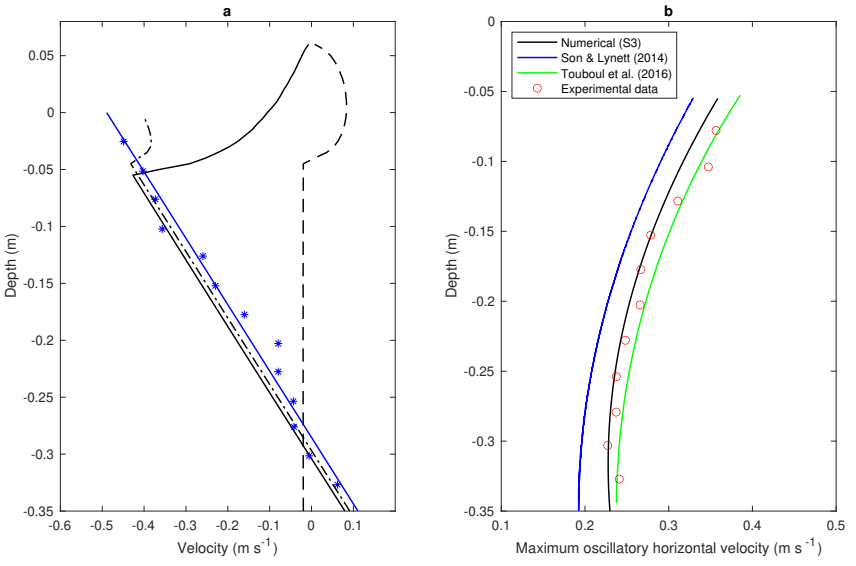

FIGURE 12. (a) For case 3, the asterisks ($***$) represent experimental data for the prescribed current; the blue line denotes the linear interpolation of experimental current data; the vertical black dashed line denotes the time-averaged velocity under the wave-alone condition; the black dashed-dotted line represents the linear superposition of velocity profiles for current-alone and wave-alone; the black line represents the numerical results from the $S3$ model for the time-averaged velocity with the consideration of wave–current interactions. (b) Comparisons of the maximum oscillatory horizontal velocities below the wave trough for case 3.

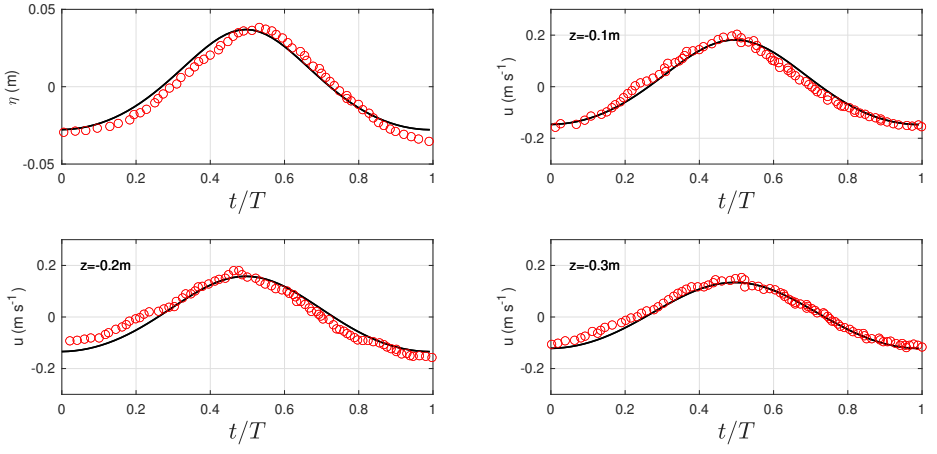

FIGURE 13. Time series of free surface elevations and oscillatory horizontal velocities for case 1 (wave following a depth-uniform current). Red circles, experimental data (Swan 1990); black line, numerical results ($S2$).

The spatial and temporal resolutions used in the numerical simulations are $\Delta x = L_w/47$ and $\Delta t = T/58$, respectively, where T is the wave period and L_w is the wavelength, estimated from linear wave theory without the consideration of current. In case 1, $kh = 0.88$, and the $S2$ model is sufficient to describe the frequency dispersion effects (see YL20). However, $S3$ model is needed for cases 2 and 3 because of their larger kh and ka values.

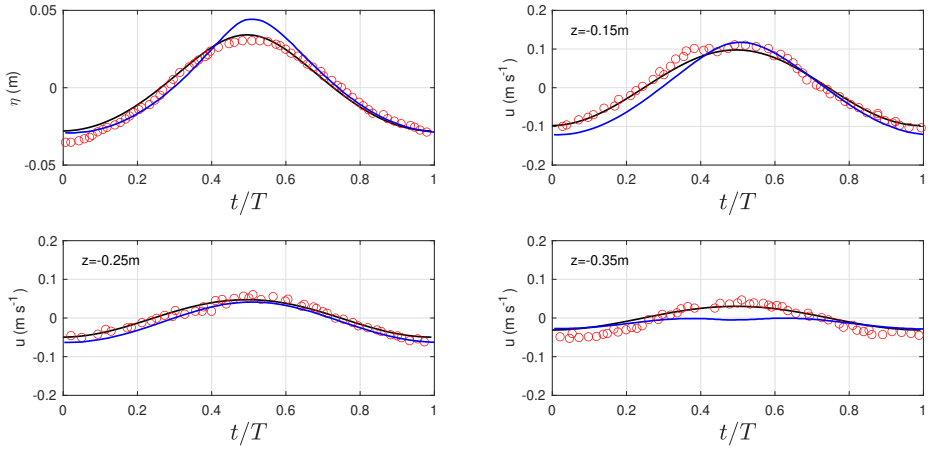

FIGURE 14. Time series of free surface elevations and oscillatory horizontal velocities for case 2 (wave with an opposing depth-uniform current). Red circles, experimental data (Swan 1990); black line, numerical results ($S3$); blue line, Boussinesq model (Son & Lynett 2014).

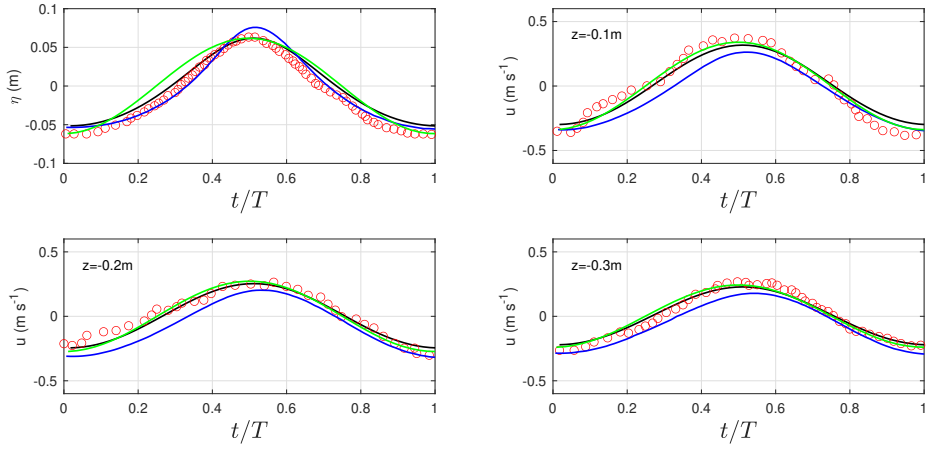

FIGURE 15. Time series of free surface elevations and oscillatory horizontal velocities for case 3 (wave with a linearly sheared opposing current). Red circles, experimental data (Swan 1990); black line, numerical results ($S3$); blue line, Boussinesq model (Son & Lynett 2014); green line, mild-slope model (Touboul *et al.* 2016).

The numerical solutions quickly reach a quasi-steady and uniform state in the region about $6L_w$ away from the internal wavemaker location. To analyze both free surface elevations and horizontal velocities, the time series of ten waves are phase-averaged and then time-averaged. The oscillatory velocity is obtained by subtracting the time-averaged values from the phase-averaged time series. From figures 13 to 15 model/data comparisons for the free surface elevations and oscillatory horizontal velocities at different water depths are shown. For case 1, the solutions from the $S2$ model and the Boussinesq model (Son & Lynett 2014) are practically identical. Thus, only the results from the present model are plotted in figure 13, showing very good agreement with the experimental data for both free surface elevations and horizontal velocities at different depths. For cases 2 and 3, the $S3$ model shows better overall skills than the Boussinesq model as indicated in figures 14 and 15.

The comparison of the vertical profiles of the maximum oscillatory horizontal velocity

for case 3 is depicted in figure 12(b), in which only the profiles below the wave trough are shown. The agreement between the $S3$ model results and experimental data is very good while the Boussinesq model underestimates the maximum oscillatory horizontal velocity. The results from the linear mild-slope equations (Touboul *et al.* 2016) are also shown in green lines for case 3 in figures 12(b) and 15. It can be observed that the linear model predicts slightly larger maximum oscillatory horizontal velocities compared with present models. In figure 12(a) the vertical profile of the time-averaged horizontal velocity calculated from the $S3$ model is shown by the full black line. Also shown in the figure is the time-averaged velocity obtained from wave-alone simulations (the vertical black dashed line). The small negative mean current is due to the numerical wave generation mechanism. A more detailed discussion can be found in Appendix B. The black dashed-dotted line is the linear superposition of the current-alone and the wave-alone solutions. Note that the prescribed steady-state current is only known up to the still water level. Below the wave trough, the time-averaged horizontal velocity under wave–current interaction (full black line) is stronger (in magnitude) than that of the linear superposition of current-alone and wave-alone solutions (black dash-dotted line), which indicates that the current is being enhanced by the nonlinear wave–current interaction for this case. Strikingly different time-averaged horizontal velocity profiles can be observed between wave trough and wave crest, suggesting that the prescribed current is strongly altered by the presence of water waves in this region. Lastly, it is found that the sum of the time-averaged and depth-integrated volume flux in the water column induced by the prescribed current and that associated with the wave-alone is almost the same as the numerical results of wave–current interactions, and the difference is less than 1%, indicating that the time-averaged volume flux across the entire water column is conserved.

C. Depth-integrated horizontal momentum equations

For demonstration purposes, the vertically independent variables mentioned in Appendix A are shown in one-dimensional form here, i.e., $i = 1$, where the superscript of H and U_m denotes the order of differentiation with respect to x and t, respectively, e.g., $U_n^{(1,0)} = \frac{\partial U_n}{\partial x}$, $U_n^{(0,1)} = \frac{\partial U_n}{\partial t}$, and $f' = \frac{\partial f}{\partial x}$.

$$H_m^w = \frac{H^{(0,1)}U_m}{H} - \frac{mH^{(0,1)}U_m}{H} + {U_m}^{(0,1)} \tag{C.1}$$

$$H_{m,n}^w = \frac{H^{(1,0)}U_mU_n}{nH} - \frac{mH^{(1,0)}U_mU_n}{nH} + {U_m}^{(1,0)}U_n + \frac{U_m{U_n}^{(1,0)}}{n} - \frac{mU_m{U_n}^{(1,0)}}{n} \tag{C.2}$$

$$H_m^{wc1} = f'U_m + f{U_m}^{(1,0)} \tag{C.3}$$

$$H_m^{wc2} = -\frac{fH^{(1,0)}U_m}{mH} - \frac{f{U_m}^{(1,0)}}{m} \tag{C.4}$$

$$H_m^{wc3} = -mf'U_m + f'U_m + \frac{fH^{(1,0)}U_m}{H} - \frac{mfH^{(1,0)}U_m}{H} \tag{C.5}$$

$$H_m^{c1} = -\frac{f^2H^{(1,0)}}{H} - ff' \tag{C.6}$$

$$H_m^{c2} = ff' \tag{C.7}$$

$$H_m^{c3} = -\frac{fH^{(0,1)}}{H} \tag{C.8}$$

$$V_m^{w1} = \frac{mh'H^{(0,1)}U_m}{H} - \frac{h'H^{(0,1)}U_m}{H} - h'{U_m}^{(0,1)} \tag{C.9}$$

$$\begin{aligned} V_m^{w2} = {} & \frac{H^{(0,1)}H^{(1,0)}U_m}{H} + H^{(1,0)}{U_m}^{(0,1)} - \frac{H^{(1,0)}{U_m}^{(0,1)}}{m} - \frac{mH^{(0,1)}H^{(1,0)}U_m}{H} \\ & + H^{(0,1)}{U_m}^{(1,0)} + H^{(1,1)}U_m - \frac{H^{(0,1)}{U_m}^{(1,0)}}{m} - \frac{H^{(1,1)}U_m}{m} - \frac{H{U_m}^{(1,1)}}{m} \end{aligned} \tag{C.10}$$

$$\begin{aligned} V_{m,n}^{w1} = {} & \frac{mh'H^{(1,0)}U_mU_n}{nH} - \frac{h'H^{(1,0)}U_mU_n}{nH} - h'{U_m}^{(1,0)}U_n \\ & + \frac{mh'U_m{U_n}^{(1,0)}}{n} - h''U_mU_n - \frac{h'U_m{U_n}^{(1,0)}}{n} \end{aligned} \tag{C.11}$$

$$\begin{aligned} V_{m,n}^{w2} = {} & \frac{(H^{(1,0)})^2U_mU_n}{nH} - \frac{m(H^{(1,0)})^2U_mU_n}{nH} + \frac{H^{(1,0)}{U_m}^{(1,0)}U_n}{n} + H^{(1,0)}{U_m}^{(1,0)}U_n \\ & + \frac{H^{(1,0)}U_m{U_n}^{(1,0)}}{n} - \frac{2H^{(1,0)}{U_m}^{(1,0)}U_n}{m} - \frac{mH^{(1,0)}U_m{U_n}^{(1,0)}}{n} + H^{(2,0)}U_mU_n \\ & - \frac{H^{(2,0)}U_mU_n}{m} + \frac{H{U_m}^{(1,0)}{U_n}^{(1,0)}}{n} - \frac{H{U_m}^{(2,0)}U_n}{m} \end{aligned} \tag{C.12}$$

$$V_m^{wc1} = -f'h'U_m - fh'{U_m}^{(1,0)} - 2fh''U_m \tag{C.13}$$

$$\begin{aligned} V_m^{wc2} = {} & \frac{f'H^{(1,0)}U_m}{m} + f'H^{(1,0)}U_m + \frac{f'H{U_m}^{(1,0)}}{m} + fH^{(1,0)}{U_m}^{(1,0)} \\ & - \frac{2fH^{(1,0)}{U_m}^{(1,0)}}{m} + 2fH^{(2,0)}U_m - \frac{fH^{(2,0)}U_m}{m} - \frac{fH{U_m}^{(2,0)}}{m} \end{aligned} \tag{C.14}$$

$$V_m^{wc3} = \frac{fh'H^{(1,0)}U_m}{mH} + \frac{fh'{U_m}^{(1,0)}}{m} \tag{C.15}$$

$$V_m^{wc4} = -\frac{f(H^{(1,0)})^2U_m}{mH} - \frac{fH^{(1,0)}{U_m}^{(1,0)}}{m} \tag{C.16}$$

$$V_m^{wc5} = f'h'\left(-U_m\right) + mf'h'U_m + \frac{mfh'H^{(1,0)}U_m}{H} - \frac{fh'H^{(1,0)}U_m}{H} \tag{C.17}$$

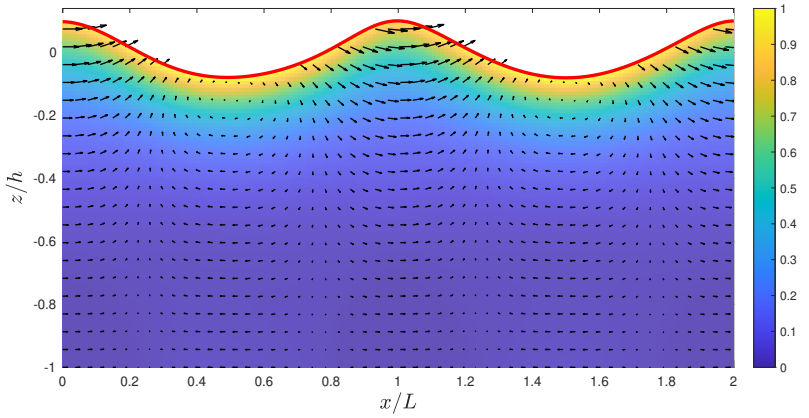

FIGURE 16. The velocity field (arrows) and vorticity field (color) for waves on following current with an exponential profile. Both waves and currents are moving to the right.

$$V_m^{wc6} = -mf'H^{(1,0)}U_m - f'H^{(1,0)}U_m + f'HU_m{}^{(1,0)} - f''HU_m + \frac{f(H^{(1,0)})^2U_m}{H} - \frac{mf(H^{(1,0)})^2U_m}{H} + fH^{(1,0)}U_m{}^{(1,0)} - fH^{(2,0)}U_m \quad \text{(C.18)}$$

$$V_m^{c1} = f'H^{(0,1)} + fH^{(1,1)} \quad \text{(C.19)}$$

$$V_m^{c2} = -ff'H^{(1,0)} + (f')^2H - ff''H - f^2H^{(2,0)} \quad \text{(C.20)}$$

$$V_m^{c3} = -f^2h'' - ff'h' \quad \text{(C.21)}$$

$$V_m^{c4} = ff'h' + \frac{f^2h'H^{(1,0)}}{H} \quad \text{(C.22)}$$

$$V_m^{c5} = ff'H^{(1,0)} + f^2H^{(2,0)} \quad \text{(C.23)}$$

$$V_m^{c6} = \frac{fh'H^{(0,1)}}{H} \quad \text{(C.24)}$$

$$V_m^{c7} = -f'H^{(0,1)} - fH^{(1,1)} \quad \text{(C.25)}$$

$$V_m^{c8} = -\frac{fH^{(0,1)}H^{(1,0)}}{H} \quad \text{(C.26)}$$

$$V_m^{c9} = -ff'H^{(1,0)} - \frac{f^2(H^{(1,0)})^2}{H} \quad \text{(C.27)}$$

D. Finite amplitude periodic waves on arbitrarily sheared currents

In the main body of the paper, we have discussed the velocity and vorticity field of finite amplitude periodic waves on opposing currents with exponential and sinusoidal profiles in the vertical direction. Here, we present the resulting velocity and vorticity field of finite amplitude waves on the following currents of the same vertical profiles.

Figure 16 shows the calculated velocity (arrows) and vorticity (color) field in a horizontal distance of two wavelengths for waves on following currents. Since the current with an exponential profile is rather weak in the lower part of the water column, the velocities are basically wave-induced orbital motions and the corresponding vorticity is almost zero. However, near the free surface, the horizontal velocity is being largely enhanced under the wave crest and it is close to zero under the wave trough. Compared with the scenario when waves propagating against the current, although the resulting velocity field is quite different, the vorticity field shows similar patterns. For the case of waves on the following

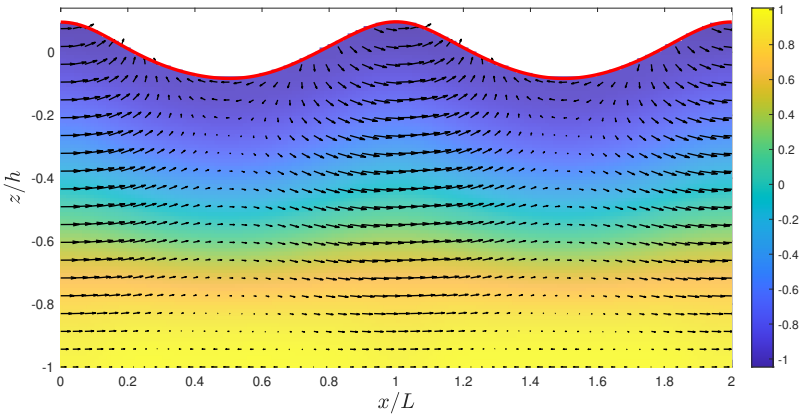

FIGURE 17. The velocity field (arrows) and vorticity field (color) for waves on following currents with a sinusoidal profile. Both waves and currents are moving to the right.

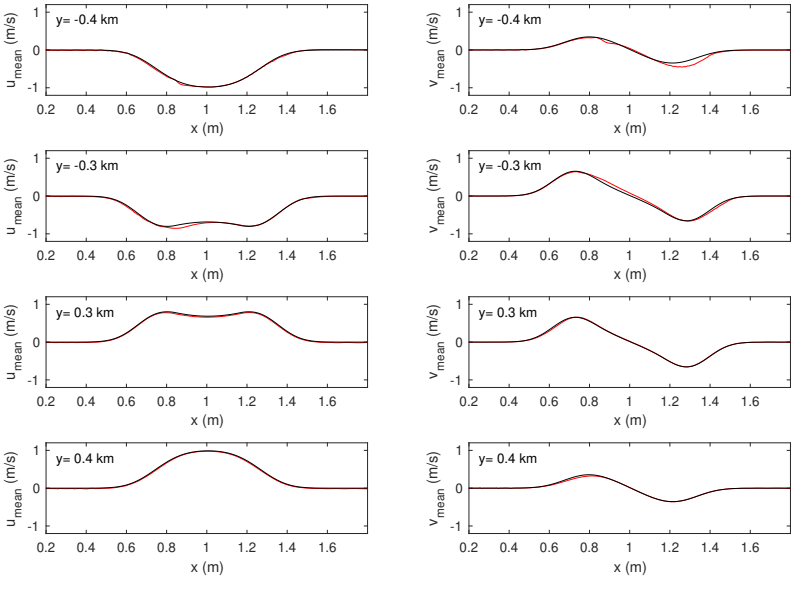

FIGURE 18. Comparisons between the time-averaged resulting current field (red line) and the prescribed current field (black line) at four transects for x component velocity, u (left panel) and y component velocity, v (right panel) at $z/h = -0.2$.

current with a sinusoidal profile, the resulting velocity and vorticity field are shown in figure 17. It can be observed that the originally horizontal uniform current is being redistributed by the presence of surface waves. While the maximum horizontal velocity occurs approximately at $z/h = -0.4$ under the wave crest, the horizontal velocity is zero at $z/h = -0.28$ and $z/h = -0.85$ under the wave trough.

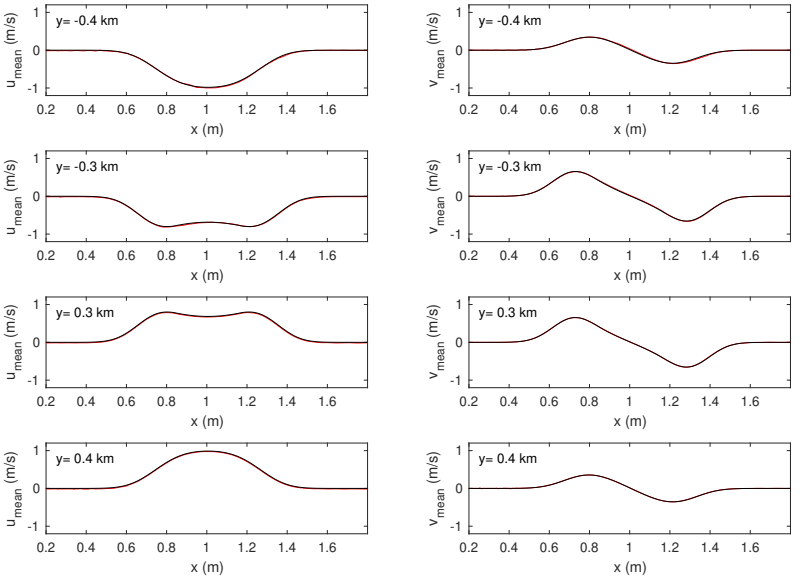

FIGURE 19. Comparisons between the time-averaged resulting current field (red line) and the prescribed current field (black line) at four transects for x component velocity, u (left panel) and y component velocity, v (right panel) at $z/h = -0.5$.

E. Wave propagation over a vortex-ring-like current

For the finite amplitude waves in the intermediate water depth case, the steady current velocities from the present model are obtained by time-averaging the total horizontal velocities over the last five waves in the simulations. The comparisons between the model results and the original vortex-ring-like current along four transects at elevations of $z/h = -0.2$ and 0.5 are shown in figure 18 and 19, respectively. It is found that the resulting current field is almost not affected by the wave field with only slight differences occur at $y = -0.4$ km and $y = -0.3$ km at the elevation of $z/h = -0.2$. The above observations show that although the current is in the same order of magnitude of wave orbital motion, the impact from waves on the current field is still weak.

REFERENCES

BERKHOFF, J. C.W., BOOY, N. & RADDER, A.C. 1982 Verification of numerical wave propagation models for simple harmonic linear water waves. *Coast. Engng* **6**, 255–279.

BOUWS, E., GÜNTHER, H., ROSENTHAL, W., VINCENT, C. L., GUNTHER, H., ROSENTHAL, W. & VINCENT, C. L. 1985 Similarity of the wind wave spectrum in finite depth water 1. Spectral form. *J. Geophys. Res.* **90**, 975–986.

BRIGGS, M.J., SYNOLAKIS, C.E. & HARKINS, G.S. 1994 Tsunami runup on a conical island. In *Proc. Waves—Physical Numer. Model.*, pp. 446–455. Vancouver, Canada: University of British Columbia.

CHAWLA, A., ÖZKAN-HALLER, H. T. & KIRBY, J. T. 1998 Spectral model for wave transformation and breaking over irregular bathymetry. *J. Waterw. Port, Coast. Ocean Eng.* **124**, 189–198.

CHOI, B. H., KIM, D. C., PELINOVSKY, E. & WOO, S. B. 2007 Three-dimensional simulation of tsunami run-up around conical island. *Coast. Engng* **54**, 618–629.

Ding, Y., Wang, S.Y. & Jia, Y. 2006 Development and validation of a quasi-three-dimensional coastal area morphological model. *J. Waterw. Port, Coast. Ocean Eng.* **132**, 462–476.

Fuhrman, D. R. & Madsen, P. A. 2008 Simulation of nonlinear wave run-up with a high-order Boussinesq model. *Coast. Engng* **55**, 139–154.

Goda, Y. 2000 *Random Seas and Design of Maritime Structures*. World Scientific Publishing Company.

Holthuijsen, L. H., Herman, A. & Booij, N. 2003 Phase-decoupled refraction-diffraction for spectral wave models. *Coast. Engng* **49**, 291–305.

Kazolea, M., Delis, A. I., Nikolos, I. K. & Synolakis, C. E. 2012 An unstructured finite volume numerical scheme for extended 2D Boussinesq-type equations. *Coast. Engng* **69**, 42–66.

Lannes, D. & Marche, F. 2015 A new class of fully nonlinear and weakly dispersive Green-Naghdi models for efficient 2D simulations. *J. Comput. Phys.* **282**, 238–268.

Liu, P. L.-F., Cho, Y. S., Briggs, M. J., Kanoglu, U. & Synolakis, C. E. 1995 Runup of solitary waves on a circular Island. *J. Fluid Mech.* **302**, 259–285.

Lynett, P. & Liu, P. L.-F. 2004 A two-layer approach to wave modelling. *Proc. Math. Phys. Eng. Sci.* **460**, 2637–2669.

Lynett, P. J., Wu, T. R. & Liu, P. L.-F. 2002 Modeling wave runup with depth-integrated equations. *Coast. Engng* **46**, 89–107.

Ma, G., Shi, F. & Kirby, J. T. 2012 Shock-capturing non-hydrostatic model for fully dispersive surface wave processes. *Ocean Model.* **43-44**, 22–35.

Mase, H. 2001 Multi-directional random wave transformation model based on energy balance equation. *Coast. Eng. J.* **43**, 317–337.

Pancbang, V. G., Wei, G., Pearce, B. R. & Briggs, M. J. 1990 Numerical simulation of irregular wave propagation over shoal. *J. Waterw. Port, Coast. Ocean Eng.* **116**, 324–340.

Son, S. & Lynett, P. J. 2014 Interaction of dispersive water waves with weakly sheared currents of arbitrary profile. *Coast. Engng* **90**, 64–84.

Swan, C. 1990 An experimental study of waves on a strongly sheared current profile. In *Coast. Eng.*, pp. 489–502.

Titov, V. V. & Synolakis, C. E. 1998 Numerical modeling of tidal wave runup. *J. Waterw. Port, Coast. Ocean Eng.* **124**, 157–171.

Touboul, J., Charland, J., Rey, V. & Belibassakis, K. 2016 Extended mild-slope equation for surface waves interacting with a vertically sheared current. *Coast. Eng.* **116**, 77–88.

Vincent, C. L. & Briggs, M. J. 1989 Refraction-diffraction of irregular waves over a mound. *J. Waterw. Port, Coast. Ocean Eng.* **115**, 269–284.

Wei, G., Kirby, J. T. & Sinha, A. 1999 Generation of waves in Boussinesq models using a source function method. *Coast. Engng* **36**, 271–299.

Whalin, R.W. 1971 The limit of applicability of linear wave refraction theory in a convergence zone. *Tech. Rep.*. H-71-3, USACE, Waterways Expt. Station, Vicksburg, MS.

Yuan, H. & Wu, C. H. 2005 Fully nonhydrostatic modeling of surface waves. *J. Eng. Mech.* **132**, 447–456.